

Quantum diamond microscopy with sub-ms temporal resolution

Sangwon Oh,^{1, a)} Seong-Joo Lee,¹ Jeong Hyun Shim,^{1, 2} Nam Woong Song,¹ and Truong Thi Hien¹

¹⁾ Quantum Magnetic Imaging Team, Korea Research Institute of Standards and Science, Daejeon 34113, South Korea

²⁾ Department of Applied Measurement Science, University of Science and Technology, Daejeon 34113, South Korea

(Dated: 18 January 2023)

Quantum diamond magnetometers using lock-in detection have successfully detected weak bio-magnetic fields from neurons, a live mammalian muscle, and a live mouse heart. This opens up the possibility of quantum diamond magnetometers visualizing microscopic distributions of the bio-magnetic fields. Here, we demonstrate a lock-in-based wide-field quantum diamond microscopy, achieving a mean volume-normalized per pixel sensitivity of $43.9 \text{ nT} \cdot \mu\text{m}^{1.5}/\text{Hz}^{0.5}$. We obtain the sensitivity by implementing a double resonance with hyperfine driving and magnetic field alignment along the $\langle 001 \rangle$ orientation of the diamond. Additionally, we have demonstrated that sub-ms temporal resolution ($\sim 0.4 \text{ ms}$) can be achieved at a micrometer scale with tens of nanotesla per-pixel sensitivity using quantum diamond microscopy. This lock-in-based diamond quantum microscopy could be a step forward in mapping functional activity in neuronal networks in micrometer spatial resolution.

I. INTRODUCTION

A nitrogen-vacancy (NV) center in diamond is an atomic defect, in which magnetic sensitivity is in the range of several microtesla with the nanometer spatial resolution at room temperature^{1,2}. The magnetic field sensitivity even reaches below $1 \text{ pT}/\text{Hz}^{0.5}$ by adopting NV ensembles at the cost of the spatial resolution³⁻⁶. Various techniques such as high-density NV centers³, improved readout fidelity^{4,7,8}, and flux concentrators^{5,6} have been implemented to improve sensitivity. These techniques have contributed to the detection of bio-magnetic fields from neurons, mammalian muscles, and a heart using NV ensembles^{3,9,10}. However, these measurements exhibit millimeter-scale spatial resolutions, which may limit the visualization of functional activity in neural networks¹¹⁻¹³. A widefield NV microscope based on the frequency shift of optically detected magnetic resonance (ODMR) can be an alternative method for detecting magnetic field distributions at a micrometer-scale spatial resolution¹⁴⁻¹⁷. Currently, density distribution in graphene, magnetic field arising from an integrated circuit, a 2-D magnet, geological samples, and living cells were imaged at sub- or several-micrometer spatial resolutions¹⁸⁻²². However, the widefield NV microscopes based on the ODMR frequency shift may have difficulties in detecting several tens of nanotesla, which corresponds to several hundreds of Hz in the frequency shift. This can be addressed using lock-in-based NV magnetometry²³.

In this study, we adopt a lock-in camera to improve the magnetic field sensitivity in a wide-field NV microscope²⁴⁻²⁷. For a simple yet reliable operation, we continuously excite NV diamond using a 532nm laser and a microwave. Multiple hyperfine transitions are simultane-

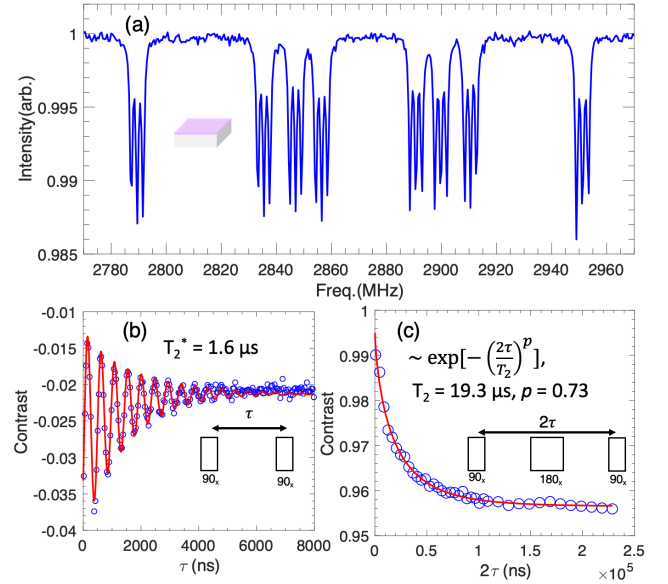


FIG. 1. ODMR spectrum and decoherence times of the overgrown diamond layer. The ODMR spectrum(a), and decoherence times, T_2^* (b) and T_2 (c), support the high quality of the crystal.

ously excited for a higher ODMR contrast, and double resonance is implemented to suppress the influences of temperature drift and strain^{3,5,25,28-30}. Additionally, all four NV axes are exploited by aligning an external magnetic field along the $\langle 001 \rangle$ direction of the NV diamond. Sub-millisecond temporal resolution, 0.4 ms, is demonstrated by detecting a magnetic field from a short-pulsed current at tens of nanotesla per-pixel sensitivity.

^{a)}sangwon.oh@kriss.re.kr

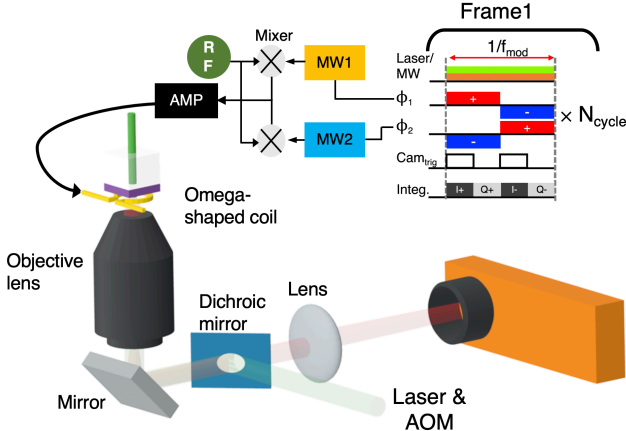


FIG. 2. (a) Schematic of the widefield microscope and protocol for lock-in camera detection. Frequency modulated (square wave) microwave (MW) is delivered into an omega-shaped coil for lock-in detection. Two MW sources (MW1 and MW2) and one RF (2.16 MHz) generator are mixed and combined for double resonance and hyperfine driving. A continuous-wave (CW) double resonance lock-in protocol is described in the inset. Phases (Φ_1 and Φ_2) of the frequency modulation are synchronized to a camera trigger for signal integration (I^+ , Q^+ , I^- , and Q^-). For magnetic field/temperature detections, $|\Phi_1 - \Phi_2|$ were kept at $\pi/0$, respectively. The trigger, Cam_{trig} , starts the acquisition of the fluorescence, and a single frame of in-phase ($I = I^+ - I^-$) and quadrature ($Q = Q^+ - Q^-$) images are found after repeating N_{cycle} times.

II. EXPERIMENTAL

A thin nitrogen-doped ($[^{14}\text{N}] \sim 10$ ppm) diamond layer ($^{12}\text{C} > 99.99\%$, $40 \mu\text{m}$ thick) is grown by chemical vapor deposition (CVD) on top of an electronic grade diamond plate by Applied Diamond Inc.. The dimensions of the diamond plate are approximately $2 \times 2 \times 0.54 \text{ mm}^3$. The diamond is electron irradiated (1 MeV , $5 \times 10^8/\text{cm}^2$), and annealed in a vacuum at 800°C for 4 hours and 1000°C for 2 hours, sequentially. An ODMR spectrum of the crystal is shown in Fig. 1(a). The NV decoherence times, T_2^* and T_2 , are found to be $1.6 \mu\text{s}$ and $19.3 \mu\text{s}$ at $B \approx 3 \text{ mT}$, respectively. T_2^* is found by fitting the data to $C_0 \exp[-(\tau/T_2^*)] \sum_i \cos[\omega_i \tau]$, where C_0 is the maximal ODMR contrast, and ω_i is frequency due to the NV hyperfine splittings, Fig. 1(b). Similarly, T_2 is obtained by fitting the data to $C_0 \exp[-(2\tau/T_2)^p]$, where p is stretched exponential parameter, Fig. 1(c)^{27,31}.

A schematic of the experimental setup is shown in Fig. 2. An omega-shaped coil is placed on the overgrown diamond layer and a 532 nm laser (Opus 3W, LaserQuantum) illuminates the diamond. The incident light power on the diamond was approximately 200 mW. An objective lens (MPLFN50x, Olympus) is used to collect the red fluorescence from the diamond. Long pass (BLP01-633R, Semrock) and dichroic (LM01-552, Semrock) filters are placed before the lock-in camera (heliCam C3,

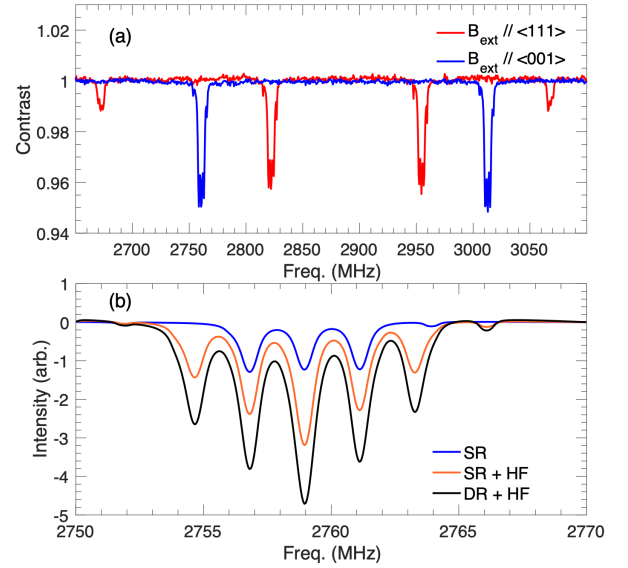


FIG. 3. ODMR spectra at two aligned cases. (a) ODMR spectra, bias fields aligned along $\langle 111 \rangle$ and $\langle 001 \rangle$ of the crystal axes; (b) ODMR of the $\langle 001 \rangle$ aligned case (SR) compared to the case of hyperfine driving (SR + HF). The contrast of the SR + HF case is enhanced by 2.4 times due to the HF driving. The contrast is further increased by adopting double resonance (DR + HF) with the same phase

Heliotis) to separate the 532-nm pump laser. We use two microwave generators (SG394, SRS) and a single RF source (2.16 MHz, WX1282C, Tabor Elec.) for the double resonance with hyperfine driving. Each SG394 was mixed (ZX05-43MH+, mini-circuits) with WX1282C and then the outputs are combined (ZX10-2-42S+, mini-circuits) for the double resonance with hyperfine driving. The mixed and combined signals are sent to an amplifier (ZHL-16W43-S+, mini-circuits). A switch (ZASWA-2-50DRA+, mini-circuits) is placed before the amplifier to control the delivery of the microwave to the omega-shaped coil. A TTL pulse generator (PB24-100-4k-PCI, spincore) is used to control the switch. A frequency modulation (square wave) is selected for the lock-in detection. The modulation depth is 300 kHz and the modulation frequencies (f_{mod}) are 2.5 or 10 kHz, depending on the temporal resolution³². The phases (ϕ_1, ϕ_2) of the frequency modulation are controlled using an arbitrary waveform generator (AWG, 33522B, Keysight). For magnetic field and temperature detections, their phase differences are maintained at 180° and 0° , respectively. The phases used for imaging magnetic fields are shown in Fig. 2. An external trigger for the camera (Cam_{trig}) comes from the TTL pulse generator and is synchronized to the phases. The trigger internally initiates an integration of the fluorescence signals during four periods, (I^+ , Q^+ , I^- , and Q^-). The in-phase ($I = I^+ - I^-$) and quadrature ($Q = Q^+ - Q^-$) images are automatically calculated by the camera. A single cycle is composed of four periods, and a single frame is a repetition of a single-cycle N_{cyc} times.

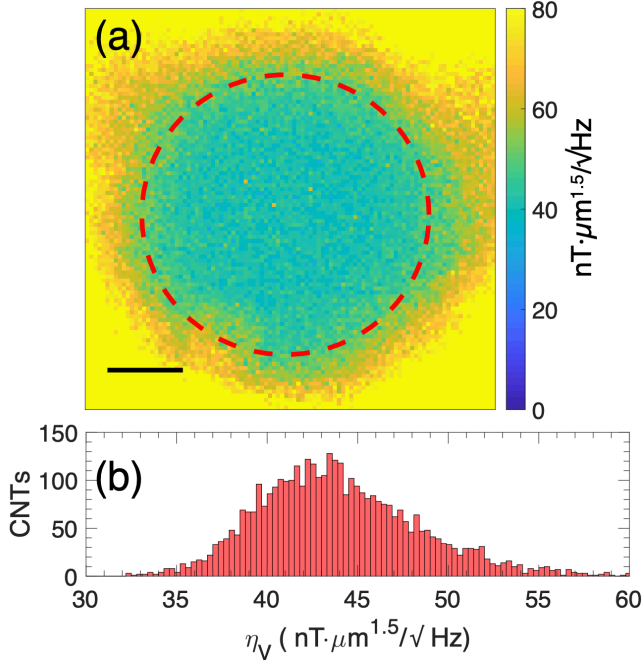


FIG. 4. Volume-normalized magnetic field sensitivity map. (a) Two-dimensional map of the volume-normalized field sensitivity, η_V and the scale bar represents $10 \mu\text{m}$; (b) A histogram of the sensitivity map within the red circled area. Mean volume sensitivity is $43.9 \text{ nT} \cdot \mu\text{m}^{1.5}/\text{Hz}^{0.5}$

The hyperfine(HF) interaction between the NV and N nuclear spin results in a reduced ODMR contrast, which is detrimental to the magnetic field sensitivity. A single frequency-sweeping ODMR spectrum due to HF interaction can be expressed as $1 - \sum_{p=-1}^1 \frac{\delta\nu^2}{\delta\nu^2 + 4(\omega - (\omega_0 + p \text{ HF}))^2}$, where $C, \nu, \omega, \omega_0, \text{HF}$ represent contrast, ODMR linewidth, applied MW frequency, resonant MW frequency, and hyperfine splitting (2.16 MHz in our case), respectively. The central contrast can be enhanced by up to three times if three equally spaced MW frequencies are swept simultaneously, $1 - \sum_{p,q=-1}^1 \frac{\delta\nu^2}{\delta\nu^2 + 4((\omega + q \text{ HF}) - (\omega_0 + p \text{ HF}))^2}$.³ In practice, the enhancement is approximately two because of power-broadened hyperfine features.

The negatively charged NV^- has an electronic spin triplet ($S = 1$) state with a temperature-dependent zero-field splitting, $D \sim 2.87 \text{ GHz}$ at room temperature, between the $|m_s = 0\rangle$ and degenerated $|m_s = \pm 1\rangle$ ³³. The degenerated states are splitted by the Zeeman effect as an external magnetic field is applied. The Hamiltonian for the NV^- in a magnetic field ($|B| > 1 \text{ mT}$) can be approximated as:^{25,34}

$$\frac{H}{h} = D(T)S_z^2 + \frac{\gamma}{2\pi}B_{NV}S_z, \quad (1)$$

where z, S_z , and B_{NV} , denote the NV symmetry axis, the dimensionless spin-1 operator, the external magnetic

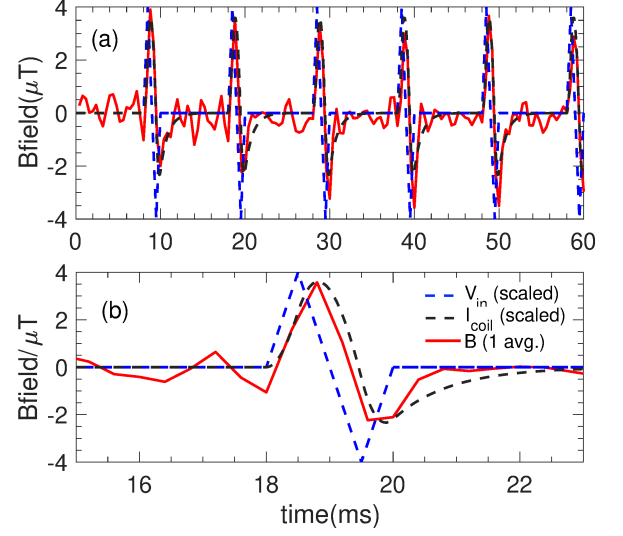


FIG. 5. Sub-ms temporal resolution. (a) A pulsed (triangular shape) voltage (dashed blue line) is applied at a coil of which inductance and resistance are 1.8 mH and 2Ω , respectively. An expected current (dashed black line) in the coil is simulated by LTspice. The measured magnetic field (solid red line), parallel to the z -axis of the crystal, is found from a single pixel in the middle of the sensitivity map in Fig. 4 (a) and shown in the upper panel. A detailed view, (b), in the time domain shows that an inductive delay in the current, $\sim 0.9 \text{ ms}$, is qualitatively captured by the magnetic field measurement.

field projected along the NV symmetry axis, and $\gamma/2\pi$ is the gyromagnetic ratio (28 GHz/T), respectively. The hyperfine interaction and spin-stress coupling parameters are ignored. The resonance frequencies can be expressed as: $f_1 = D(t) - \gamma B_{NV}(t)$ for $|m_s = 0\rangle \leftrightarrow |m_s = -1\rangle$ and $f_2 = D(t) + \gamma B_{NV}(t)$ for $|m_s = 0\rangle \leftrightarrow |m_s = 1\rangle$ where $D(t) = D_0 + \Delta D(t)$ and $B_{NV}(t) = B_{NV0} + \Delta B_{NV}(t)$.

A double resonance (DR) simultaneously drives the resonance frequencies (f_1, f_2) using two microwave generators (MW1 and MW2) with the modulation frequency (f_{mod}) and phases (ϕ_1, ϕ_2). The output signals of the lock-in amplifier at f_1 and f_2 are $S_1(t) = \alpha[\Delta D(t) - \gamma B_{NV}(t)]$ and $S_2(t) = \alpha[\Delta D(t) + \gamma B_{NV}(t)]$, respectively, where α is the slope of the lock-in amplifier. If we apply DR with the same phase, i.e. $\phi_1 = \phi_2$, then the lock-in signal (S_{LIA}) is only sensitive to the temperature, $S_{LIA} = 2\alpha\Delta D(t)$. Alternatively, it depends only on the magnetic field (ΔB_{NV}) if $|\phi_1 - \phi_2| = \pi$, $S_{LIA} = 2\alpha\Delta B(t)$ ^{5,30,35,36}. Additionally, the sensitivity of the DR method is expected to be enhanced by $\sim 4/3$ times compared to the sensitivity of the single-resonance method⁵.

III. RESULTS

The shot-noise-limited continuous wave (CW) magnetic field sensitivity, η_{CW} , is given by^{3,37}:

$$\eta_{CW} = \frac{4}{3\sqrt{3}} \frac{h}{g_e \mu_B} \frac{\Delta\nu}{C\sqrt{R}}, \quad (2)$$

where R is the photon-detection rate, $\Delta\nu$ is the linewidth, and C is the ODMR contrast. To minimize the η_{CW} , we adopt several methods to obtain a higher ODMR contrast in Eq. (2). The first method is projecting a magnetic field equally along all the NV axes. We compare the ODMR spectra where the external magnetic fields are aligned along the $\langle 111 \rangle$ and $\langle 001 \rangle$ directions of the crystal, as shown in Fig. 3(a). When the magnetic field is along the $\langle 001 \rangle$ direction of the crystal, the ODMR contrast can be maximized^{3,30}. Hereafter, we fix the external field along the $\langle 001 \rangle$ direction. The second method is to simultaneously excite the three HF features (SR + HF) instead of exciting a single frequency (SR). The ODMR contrast is improved by 2.4 times, compared to that in SR, as shown in Fig. 3(b). The third method involves applying DR along with HF driving (DR + HF). This further enhances the contrast compared to that in SR + HF, as shown in Fig. 3 (b). DR is essential for minimizing errors in the magnetic field due to temperature drift in the system²⁸⁻³⁰.

The magnetic field sensitivity can be expressed as $\eta = \delta B \sqrt{T}$, where δB is the minimum detectable magnetic field, and T is the measurement duration. The minimum magnetic field is given by the standard deviation of a series of measurements^{25,27}. To determine the minimum magnetic field, a test field is applied along the z-axis of the crystal. The test field is found to be $6.8 \mu\text{T}$, and the projected magnetic field along the NV axes is $4 \mu\text{T}$. The frame rate of the camera is 114 Hz (8.8 ms, $f_{\text{mod}} = 2.5 \text{ kHz}$, 22 cycles), and 110 frames are collected for the estimation.

A two-dimensional map of the volume-normalized magnetic field sensitivity, $\eta_V = \eta \sqrt{V}$, is shown in Fig. 4(a), where the field of view is approximately $46 \times 46 \mu\text{m}^2$, the pixel size is $0.54 \times 0.54 \mu\text{m}^2$, and the sensor volume, V , is $11.7 (0.54 \times 0.54 \times 40) \mu\text{m}^3$. The mean η_V within the red circled area is $43.9 \text{ nT} \cdot \mu\text{m}^{1.5}/\text{Hz}^{0.5}$ and the mean per pixel η is $12.8 \text{ nT}/\text{Hz}^{0.5}$. The histogram of the η_V within the area shows a Gaussian-like distribution due to the beam shape, as shown in Fig. 4 (b). Illuminating the NV diamond based on the total internal reflection is expected to result in a larger field of view and a more uniform sensitivity distribution than that in the current scheme^{7,25}.

To demonstrate a sub-millisecond temporal resolution, the frame rate is increased to 2500 Hz, and 200 frames are acquired, where the modulation frequency is set to 10 kHz. The increased modulation frequency decreases the signal-to-noise ratio due to the wider bandwidth. A series of pulsed voltages are applied to a coil with a diameter of 10 cm, an inductance of 1.8 mH, and a resistance of 2Ω . The voltage pulse has a triangular shape, and its polarity is changed within 2 ms and repeats every 10 ms, as shown in Fig. 5 (b). Because the dimensions of the

coil are significantly larger than the field of view (Fig. 4 (a)), the magnetic field produced by the pulsed voltage is uniform.

A single acquisition of the magnetic field from the voltage pulse at a single central pixel is shown in Fig. 5(a). The dashed blue line represents the applied voltage (scaled), and the dashed black line represents the expected current in the coil. The solid red line represents the magnetic field along the z-axis of the crystal. Even in a single measurement, we can distinguish $\pm 4 \mu\text{T}$ magnetic pulse trains from the noise. The expected delay between the current (magnetic field) and the voltage is approximately 0.9 (1.8/ 2) ms. A close-up in the time domain, Fig. 5(b), indicates that our system can capture the transient behavior with sub-millisecond temporal resolution. The standard deviation of the noise level ($\approx 1 \mu\text{T}$) during the acquisition duration (0.4 ms) leads to a per-pixel sensitivity of $20 \text{ nT}/\text{Hz}^{0.5}$. These observations support the nanotesla sensitivity with sub-millisecond temporal resolution.

IV. DISCUSSION

In this study, we optimize the volume-normalized magnetic field sensitivity of NV center ensembles using a lock-in camera. The mean per pixel volume-normalized magnetic field sensitivity of $43.9 \text{ nT} \cdot \mu\text{m}^{1.5}/\text{Hz}^{0.5}$ and the sub-ms temporal resolution are obtained at a relatively low optical power density of $0.12 \text{ mW}/\mu\text{m}^2$. However, we still need to improve the sensitivity to less than $1 \text{ nT} \cdot \mu\text{m}^{1.5}/\text{Hz}^{0.5}$ to visualize neuronal networks^{12,13}. In this section, we will discuss how we can further improve the magnetic field sensitivity.

Photonic structures such as diamond nano-pillars will enhance the volume-normalized sensitivity by improving readout fidelity^{38,39}. It has been reported that the sensitivity can be improved by more than four times owing to increased photoluminescence and spin coherence time by nano-pillar³⁹. An additional antireflective coating of 600 - 800 nm on the diamond further increases the photoluminescence further⁴⁰.

The inhomogeneous spin dephasing time, T_2^* , can be extended by applying decoupling sequences. The dipolar coupling between NV centers and substitutional nitrogen (P1) can be suppressed by driving P1 spins^{31,41}. Bauch *et al.* and Balasubramanian *et al.* reported that T_2^* in a high P1 density increased more than four times using spin-bath driving^{31,41}. Moreover, Balasubramanian *et al.* decoupled NV-NV interaction by adopting WAHUA sequence and additionally extended T_2^* by ten times⁴¹. These methods, combined with our technique, could reduce the volume-normalized sensitivity to less than $1 \text{ nT} \cdot \mu\text{m}^{1.5}/\text{Hz}^{0.5}$, which is an essential tool for understanding neuronal connectivity¹¹⁻¹³.

Illuminating the NV layer uniformly using total internal reflection geometry improves the magnetic sensitivity distribution and increases the field of view up to the mil-

limeter scale^{7,19}. This can be utilized to detect magnetic fields from an integrated circuit and 3-D current distribution in a multi-layer printed circuit board^{19,42}. Combined with the sub-millisecond temporal resolution, the wide field of view could contribute to imaging transient events, which could be missed by scanning-based systems such as giant-magneto resistive (GMR) or superconducting quantum interference device (SQUID)-based current mapping equipment^{19,43}.

V. CONCLUSION

In conclusion, we have obtained a mean per pixel volume-normalized magnetic sensitivity of $43.9 \text{ nT} \cdot \mu\text{m}^{1.5}/\text{Hz}^{0.5}$ and a sub-ms temporal resolution using NV center ensembles and a lock-in camera. The HF driving, DR, and exploitation of the four NV axes are adopted with CW lock-in detection to reach the sensitivity. These methods could be a step forward for visualizing microscopic distributions of sub-nanotesla changes due to neuronal currents in real-time, as well as defects in a packaged battery⁴⁴.

DECLARATIONS

Acknowledgments

The authors thank Kiwoong Kim for valuable discussions and Heloitis AG for experimental assistance in implementing the camera.

Funding

This research was supported by Institute of Information & communications Technology Planning & Evaluation (IITP) grants funded by the Korea government (MSIT) (No.2019-000296, No.2021-0-00076) and a grant (GP2021-0010) from Korea Research Institute of Standards and Science.

Availability of data and materials

The data that support the findings of this study are available from the corresponding author upon reasonable request.

- ¹J. M. Taylor, P. Cappellaro, L. Childress, L. Jiang, D. Budker, P. R. Hemmer, A. Yacoby, R. Walsworth, and M. D. Lukin, *Nature Physics* **4**, 810 (2008).
- ²J. R. Maze, P. L. Stanwix, J. S. Hodges, S. Hong, J. M. Taylor, P. Cappellaro, L. Jiang, M. V. G. Dutt, E. Togan, A. S. Zibrov, A. Yacoby, R. L. Walsworth, and M. D. Lukin, *Nature* **455**, 644 (2008).

- ³J. F. Barry, M. J. Turner, J. M. Schloss, D. R. Glenn, Y. Song, M. D. Lukin, H. Park, and R. L. Walsworth, *Proceedings of the National Academy of Sciences* **113**, 14133 (2016), <https://www.pnas.org/doi/pdf/10.1073/pnas.1601513113>.
- ⁴T. Wolf, P. Neumann, K. Nakamura, H. Sumiya, T. Ohshima, J. Isoya, and J. Wrachtrup, *Phys. Rev. X* **5**, 041001 (2015).
- ⁵I. Fescenko, A. Jarmola, I. Savukov, P. Kehayias, J. Smits, J. Damron, N. Ristoff, N. Mosavian, and V. M. Acosta, *Phys. Rev. Research* **2**, 023394 (2020).
- ⁶C. Zhang, F. Shagieva, M. Widmann, M. Kübler, V. Vorobyov, P. Kapitanova, E. Nenasheva, R. Corkill, O. Rhrle, K. Nakamura, H. Sumiya, S. Onoda, J. Isoya, and J. Wrachtrup, *Phys. Rev. Applied* **15**, 064075 (2021).
- ⁷H. Clevenson, M. E. Trusheim, C. Teale, T. Schröder, D. Braje, and D. Englund, *Nature Physics* **11**, 393 (2015).
- ⁸Y. Dumeige, M. Chipaux, V. Jacques, F. Treussart, J.-F. Roch, T. Debuisschert, V. M. Acosta, A. Jarmola, K. Jensen, P. Kehayias, and D. Budker, *Phys. Rev. B* **87**, 155202 (2013).
- ⁹J. L. Webb, L. Troise, N. W. Hansen, C. Olsson, A. M. Wojciechowski, J. Achard, O. Brinza, R. Staacke, M. Kieschnick, J. Meijer, A. Thielscher, J.-F. Perrier, K. Berg-Sørensen, A. Huck, and U. L. Andersen, *Scientific Reports* **11**, 2412 (2021).
- ¹⁰K. Arai, A. Kuwahata, D. Nishitani, I. Fujisaki, R. Matsuki, Z. Xin, Y. Nishio, X. Cao, Y. Hatano, S. Onoda, C. Shinei, M. Miyakawa, T. Taniguchi, M. Yamazaki, T. Teraji, T. Ohshima, M. Hatano, M. Sekino, and T. Iwasaki, *arXiv:2105.11676* (2021).
- ¹¹L. T. Hall, G. C. G. Beart, E. A. Thomas, D. A. Simpson, L. P. McGuinness, J. H. Cole, J. H. Manton, R. E. Scholten, F. Jelezko, J. Wrachtrup, S. Petrou, and L. C. L. Hollenberg, *Scientific Reports* **2**, 401 (2012).
- ¹²M. Karadas, A. M. Wojciechowski, A. Huck, N. O. Dalby, U. L. Andersen, and A. Thielscher, *Scientific Reports* **8**, 4503 (2018).
- ¹³M. Karadas, C. Olsson, N. Winther Hansen, J.-F. Perrier, J. L. Webb, A. Huck, U. L. Andersen, and A. Thielscher, *Frontiers in Neuroscience* **15** (2021), 10.3389/fnins.2021.643614.
- ¹⁴S. Steinert, F. Dolde, P. Neumann, A. Aird, B. Naydenov, G. Balasubramanian, F. Jelezko, and J. Wrachtrup, *Review of Scientific Instruments* **81**, 043705 (2010), <https://doi.org/10.1063/1.3385689>.
- ¹⁵D. A. Simpson, J.-P. Tetienne, J. M. McCoe, K. Ganesan, L. T. Hall, S. Petrou, R. E. Scholten, and L. C. L. Hollenberg, *Scientific Reports* **6**, 22797 (2016).
- ¹⁶D. R. Glenn, K. Lee, H. Park, R. Weissleder, A. Yacoby, M. D. Lukin, H. Lee, R. L. Walsworth, and C. B. Connolly, *Nature Methods* **12**, 736 (2015).
- ¹⁷S. C. Scholten, A. J. Healey, I. O. Robertson, G. J. Abrahams, D. A. Broadway, and J.-P. Tetienne, *Journal of Applied Physics* **130**, 150902 (2021), <https://doi.org/10.1063/5.0066733>.
- ¹⁸J.-P. Tetienne, N. Dontschuk, D. A. Broadway, A. Stacey, D. A. Simpson, and L. C. L. Hollenberg, *Science Advances* **3**, e1602429 (2017), <https://www.science.org/doi/pdf/10.1126/sciadv.1602429>.
- ¹⁹M. J. Turner, N. Langellier, R. Bainbridge, D. Walters, S. Meesala, T. M. Babinec, P. Kehayias, A. Yacoby, E. Hu, M. Lončar, R. L. Walsworth, and E. V. Levine, *Phys. Rev. Applied* **14**, 014097 (2020).
- ²⁰D. Broadway, S. Lillie, S. Scholten, D. Rohner, N. Dontschuk, P. Maletinsky, J.-P. Tetienne, and L. Hollenberg, *Phys. Rev. Applied* **14**, 024076 (2020).
- ²¹D. R. Glenn, R. R. Fu, P. Kehayias, D. Le Sage, E. A. Lima, B. P. Weiss, and R. L. Walsworth, *Geochemistry, Geophysics, Geosystems* **18**, 3254 (2017).
- ²²D. Le Sage, K. Arai, D. R. Glenn, S. J. DeVience, L. M. Pham, L. Rahn-Lee, M. D. Lukin, A. Yacoby, A. Komeili, and R. L. Walsworth, *Nature* **496**, 486 (2013).
- ²³R. S. Schoenfeld and W. Harneit, *Phys. Rev. Lett.* **106**, 030802 (2011).

- ²⁴A. M. Wojciechowski, M. Karadas, A. Huck, C. Osterkamp, S. Jankuhn, J. Meijer, F. Jelezko, and U. L. Andersen, *Review of Scientific Instruments* **89**, 031501 (2018), <https://doi.org/10.1063/1.5010282>.
- ²⁵C. A. Hart, J. M. Schloss, M. J. Turner, P. J. Scheidegger, E. Bauch, and R. L. Walsworth, *Phys. Rev. Applied* **15**, 044020 (2021).
- ²⁶J. L. Webb, L. Troise, N. W. Hansen, L. F. Frellsen, C. Osterkamp, F. Jelezko, S. Jankuhn, J. Meijer, K. Berg-Sørensen, J.-F. m. c. Perrier, A. Huck, and U. L. Andersen, *Phys. Rev. Appl.* **17**, 064051 (2022).
- ²⁷H. Park, J. Lee, S. Han, S. Oh, and H. Seo, *npj Quantum Information* **8**, 95 (2022).
- ²⁸K. Fang, V. M. Acosta, C. Santori, Z. Huang, K. M. Itoh, H. Watanabe, S. Shikata, and R. G. Beausoleil, *Phys. Rev. Lett.* **110**, 130802 (2013).
- ²⁹H. J. Mamin, M. H. Sherwood, M. Kim, C. T. Rettner, K. Ohno, D. D. Awschalom, and D. Rugar, *Phys. Rev. Lett.* **113**, 030803 (2014).
- ³⁰J. H. Shim, S.-J. Lee, S. Ghimire, J. I. Hwang, K.-G. Lee, K. Kim, M. J. Turner, C. A. Hart, R. L. Walsworth, and S. Oh, *Phys. Rev. Applied* **17**, 014009 (2022).
- ³¹E. Bauch, C. A. Hart, J. M. Schloss, M. J. Turner, J. F. Barry, P. Kehayias, S. Singh, and R. L. Walsworth, *Phys. Rev. X* **8**, 031025 (2018).
- ³²H. A. R. El-Ella, S. Ahmadi, A. M. Wojciechowski, A. Huck, and U. L. Andersen, *Opt. Express* **25**, 14809 (2017).
- ³³M. W. Doherty, F. Dolde, H. Fedder, F. Jelezko, J. Wrachtrup, N. B. Manson, and L. C. L. Hollenberg, *Phys. Rev. B* **85**, 205203 (2012).
- ³⁴P. Kehayias, M. J. Turner, R. Trubko, J. M. Schloss, C. A. Hart, M. Wesson, D. R. Glenn, and R. L. Walsworth, *Phys. Rev. B* **100**, 174103 (2019).
- ³⁵A. M. Wojciechowski, M. Karadas, C. Osterkamp, S. Jankuhn, J. Meijer, F. Jelezko, A. Huck, and U. L. Andersen, *Applied Physics Letters* **113**, 013502 (2018), <https://doi.org/10.1063/1.5026678>.
- ³⁶Y. Hatano, J. Shin, D. Nishitani, H. Iwatsuka, Y. Masuyama, H. Sugiyama, M. Ishii, S. Onoda, T. Ohshima, K. Arai, T. Iwasaki, and M. Hatano, *Applied Physics Letters* **118**, 034001 (2021), <https://doi.org/10.1063/5.0031502>.
- ³⁷A. Dréau, M. Lesik, L. Rondin, P. Spinicelli, O. Arcizet, J.-F. Roch, and V. Jacques, *Phys. Rev. B* **84**, 195204 (2011).
- ³⁸S. A. Momenzadeh, R. J. Stöhr, F. F. de Oliveira, A. Brunner, A. Denisenko, S. Yang, F. Reinhard, and J. Wrachtrup, *Nano Letters*, *Nano Letters* **15**, 165 (2015).
- ³⁹D. J. McCloskey, N. Donschuk, D. A. Broadway, A. Nadarajah, A. Stacey, J.-P. Tetienne, L. C. L. Hollenberg, S. Prawer, and D. A. Simpson, *ACS Applied Materials & Interfaces*, *ACS Applied Materials & Interfaces* **12**, 13421 (2020).
- ⁴⁰J. L. Webb, J. D. Clement, L. Troise, S. Ahmadi, G. J. Johansen, A. Huck, and U. L. Andersen, *Applied Physics Letters* **114**, 231103 (2019), <https://doi.org/10.1063/1.5095241>.
- ⁴¹P. Balasubramanian, C. Osterkamp, Y. Chen, X. Chen, T. Teraji, E. Wu, B. Naydenov, and F. Jelezko, *Nano Letters* **19**, 6681 (2019), <https://doi.org/10.1021/acs.nanolett.9b02993>.
- ⁴²S. M. Oliver, D. J. Martynowych, M. J. Turner, D. A. Hopper, R. L. Walsworth, and E. V. Levine, *International Symposium for Testing and Failure Analysis*, **ISTFA 2021: Conference Proceedings from the 47th International Symposium for Testing and Failure Analysis**, 96 (2021), <https://dl.asminternational.org/istfa/proceedings-pdf/ISTFA2021/84215/96/607202/istfa2021p0096.pdf>.
- ⁴³A. Orozco, J. Gaudestad, N. Gagliolo, C. Rowlett, E. Wong, A. Jeffers, B. Cheng, F. Wellstood, A. Cawthorne, and F. Infante, *International Symposium for Testing and Failure Analysis*, **ISTFA 2013: Conference Proceedings from the 39th International Symposium for Testing and Failure Analysis**, 189 (2013), <https://dl.asminternational.org/istfa/proceedings-pdf/ISTFA2013/80224/189/414917/istfa2013p0189.pdf>.
- ⁴⁴X. Zhang, G. Chatzidrosos, Y. Hu, H. Zheng, A. Wickenbrock, A. Jerschow, and D. Budker, *Applied Sciences* **11** (2021), 10.3390/app11073069.